PNAS RESEARCH ARTICLE | CHEMISTRY
IMMUNOLOGY AND INFLAMMATION

Viral mimicry may help explain immunogenic cell death

Matthew S. Levine[a], Jiexi Li[b], Lauren I. R. Ehrlich[c,1], Ronald A. DePinho[b,1], Brent Iverson[a,1], and Jonathan L. Sessler[a,1]

Contributed by Jonathan L. Sessler; received December 29, 2025; accepted February 4, 2026; reviewed by Jacqueline K. Barton and Gilles Gasser

Viral mimicry may be an underappreciated contributor to chemotherapeutic potency in animal models and patients. This hypothesis is based on studies of a bis-Au(I)-NHC complex that was found to generate a strong *anti-tumor immune response* in vivo in two different challenge studies using an iKAP colorectal cancer mouse model. RNA profiling of treated cells revealed the stimulation of genes that overlap with those upregulated during a viral infection. The bis-Au(I)-NHC complex generates reactive oxygen species (ROS) through the simultaneous redox cycling of the naphthoquinone moiety and inhibition of thioredoxin reductase with Au(I). This ROS increase causes endoplasmic reticulum stress, activation of the unfolded protein response pathway and upregulation of Ifih1, a gene that encodes for the viral dsRNA sensor MDA5. Activation of MDA5 triggers a strong type I interferon response and expression of chemokine ligand 10 that can recruit immune cells to the treated tumor in a manner analogous to immune responses during viral infection. This proposed mechanism bridges the gap between cytotoxicity and the innate and adaptive immune responses. We suggest viral mimicry may be a key driver of chemotherapy potency in animals and an important determinant of positive outcomes in cancer patients.

viral mimicry | cancer | immunogenic cell death

Significance

It has long been observed that cancer patients respond differently to the same cytotoxic chemotherapeutic agent. We are proposing here that cytotoxicity-induced viral mimicry contributes to so-called immunogenic cell death and could represent an underappreciated determinant of patient outcome associated with cancer chemotherapy. Viral mimicry as a proposed mechanism of action thus bridges the gap between cytotoxicity and the innate and adaptive immune responses.

Immunogenic Cell Death (ICD) is a term that has been used to indicate a type of cancer cell killing that triggers an effective anti-tumor immune response (1). Certain anthracyclines (2, 3), metal complexes (4–7), nanoparticles (8) and oncolytic viruses (9) have been found to trigger such a response. Three biomarkers have been associated with these triggering agents: (10) Calreticulin (CRT) translocation, ATP release, and high mobility group box 1 (HMGB1) secretion. This biomarker release is thought to reflect cellular activation of stress responses prior to cell death. Once these biomarkers, presumably along with others that have yet to be described, are released from a treated tumor cell, a stepwise process ensues. This process involves phagocytosis of dying/dead tumor cells by phagocytes, including dendritic cells (DCs), followed by antigen processing by mature DCs and presentation to T cells. Altogether, this cascade culminates in an IFN-γ mediated adaptive immune response involving cytotoxic T cells and γδ T cells that targets residual tumor cells (10).

For cytotoxic agents that can trigger this type of immune response, an important question concerns the role of innate immunity in the overall process. Ordinarily, an innate immune response is seen when cells become infected with pathogens, including viruses. When this occurs, inflammatory responses and ultimately cell death can be induced. Although slower, the adaptive immune response also provides a mechanism for cell killing as well as a way for the host to respond to incidences of subsequent infection by the same pathogen and mobilize a specific response in an accelerated fashion. Since immune responses are expected to vary from individual to individual, we believe patients' differential ability to harness immune responses effectively may underlie interindividual variations in the efficacy of a given anticancer therapeutic.

Recently our group showed that compound **1** (Fig. 1), a redox active Au(I) complex, induced an extremely long-lasting anti-tumor immune response in a mouse CT26 colorectal cancer cell (CRC) model compared to oxaliplatin (a known ICD inducer and positive control used for this study) (5). Au(I) complexes, such as the FDA-approved drug auranofin, only target the antioxidant network through inhibition of the selenocysteine residue of thioredoxin reductase (TrxR2), thereby hampering the cells' ability to neutralize reactive oxygen species (ROS) (11). On the other hand, compound **1** was designed to target the antioxidant network of cancer cells in two ways: First, in analogy to what is seen for auranofin, the Au(I) metal center of compound **1** is thought to react with a selenocysteine residue of TrxR2 within the mitochondria, thereby acting as a covalent inhibitor. This inhibition limits the ability of the cell to mitigate damage from ROS (11). Second, unlike auranofin, compound **1** simultaneously generates ROS in the mitochondria as the result of redox cycling involving the naphthoquinone moiety. As explained in our original report,

Author affiliations: [a]Department of Chemistry, The University of Texas at Austin, Austin, TX 78712-1224; [b]Department of Cancer Biology, The University of Texas MD Anderson Cancer Center, Houston, TX 77054.; and [c]Department of Molecular Biosciences, The University of Texas at Austin, Austin, TX 78712-0159

Author contributions: M.S.L., J.L., L.I.R.E., R.A.D., B.I., and J.L.S. designed research; M.S.L. and J.L. performed research; M.S.L., J.L., L.I.R.E., R.A.D., B.I., and J.L.S. analyzed data; and M.S.L., J.L., L.I.R.E., R.A.D., B.I., and J.L.S. wrote the paper.

Reviewers: J.K.B., California Institute of Technology; and G.G., Chimie ParisTech.

Competing interest statement: A PCT application has been filed by the University of Texas.

[1]To whom correspondence may be addressed. Email: lehrlich@austin.utexas.edu, rdepinho@mdanderson.org, iversonb@austin.utexas.edu, or sessler@cm.utexas.edu.

This article contains supporting information online at https://www.pnas.org/lookup/suppl/doi:10.1073/pnas.2537547123/-/DCSupplemental.

Published March 11, 2026.

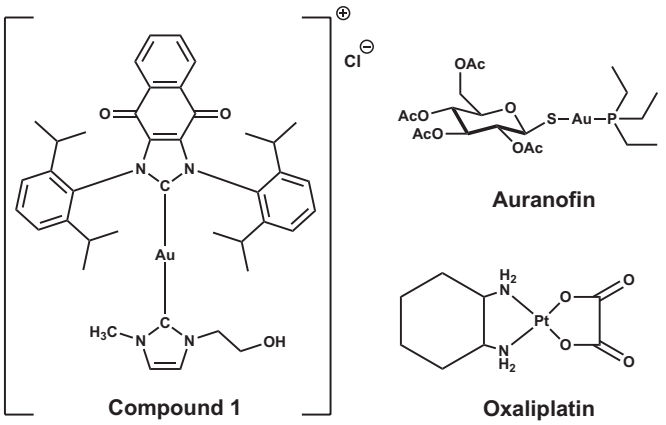

Fig. 1. Chemical structures of Au(I) and Pt(II) complexes considered in this study.

the contemporaneous generation of ROS and shutting down of the TrxR2 pathway can be thought of as turning on a faucet (ROS) while plugging the drain (TrxR2). The net result is that the "ROS sink" overflows leading to cancer cell death in this analogy. Consistent with its design, compound **1** was found to induce considerable ROS stress and presumably that is why it proved more toxic in the CT26 cell line than auranofin (5).

In the present study, we have investigated the cellular and immune responses to compound **1** in an iKAP CRC mouse syngeneic tumor model. The iKAP cell line is microsatellite stable (MSS) and has a homozygous KRAS (Kirsten rat sarcoma virus oncogene homologue) mutation ($KRAS^{G12D}$) and deletions of APC and TRP53 (12). This genetic profile faithfully recapitulates a majority of human CRCs (13). Furthermore this type of CRC does not respond to immune checkpoint inhibitors alone, such as anti-PD1, making them difficult to treat (14). We investigated the cytotoxicity, ROS generation, ICD biomarker expression, and in vivo anti-tumor adaptive immunity elicited by iKAP cells treated with compound **1**. Additionally, RNA profiling of treated iKAP cells was carried out to investigate how compound **1** might trigger immune responses.

The important result described below is that compound **1** induced a cellular RNA profile that is similar to that seen during a viral infection, a concept termed "viral mimicry" (15). Viral mimicry has been previously associated with DNA-demethylating agents, such as 5-azacytidine or zebularine (15, 16). These seminal findings along with our results lead us to suggest that innate antiviral sensing may be an underappreciated driver of an anti-tumor immune response generated by cytotoxic agents and thereby account for the elicitation of ICD.

Results

In Vitro Results. The antiproliferative activities of compound **1** as well as oxaliplatin and auranofin controls were evaluated in the mouse iKAP CRC cell line using a 72-h post treatment 3-(4,5-dimethylthiazol-2-yl)-2,5-diphenyltetrazolium bromide (MTT) assay. As shown in Fig. 2*A*, The IC_{50} values revealed that compound **1** (0.012 μM ± 0.002) was significantly more toxic than either auranofin (1.48 μM ± 0.35) or oxaliplatin (3.83 μM ± 0.48). As noted above, the large difference in toxicity between compound **1** and auranofin was expected because only compound **1** possesses the capability of generating exogenous ROS in addition to inhibiting TrxR2 (5). IKAP cells were incubated separately with compound **1**, oxaliplatin, and auranofin for 4 h. The cells were then stained with CellRox™ Orange (ThermoFisher, C10493) which is used to measure ROS inside cells. Fluorescence levels were measured by flow cytometry, and the results were gated against SYTOX™ Blue to exclude dead cells from the analysis (*SI Appendix,* Fig. S1). As seen in Fig. 2*B*, compound **1** generated higher levels of ROS compared to auranofin (or untreated cells) at the same concentration. Oxaliplatin, even at a highly elevated concentration, only generated minimal ROS.

Compound **1** was then analyzed for its ability to elicit the key ICD biomarkers CRT, ATP, and HMGB1. In these studies, untreated cells were used as a negative control. CRT translocation from the endoplasmic reticulum (ER) to the surface of the cell membrane was analyzed using confocal microscopy. Here, cells were incubated with either 10 μM of compound **1**, 10 μM of auranofin or 150 μM of oxaliplatin. Compound **1** and oxaliplatin were previously reported to induce ICD biomarkers at these concentrations (5). After incubation, cells were washed 3× with PBS and subsequently stained with anti-CRT rabbit polyclonal antibody (Invitrogen PA3-900) followed by goat anti-rabbit polyclonal antibodies labeled with Alexa Fluor 594 (color has been changed to cyan for visual clarity) (Invitrogen A-11012). The cell membrane was then stained with Wheat Germ Alexa Fluor (Cayman, 30423) (color changed to yellow for visual clarity) and the nuclear staining agent Hoechst (color changed to purple for visual clarity). As shown in Fig. 2*C*, the merged images for compound **1** at 10 μM demonstrated a higher level of colocalization of the emission signals from the CRT antibodies and the cell membrane stain. Auranofin also showed CRT translocation in this cell line. This is surprising because it is currently disputed whether auranofin is able to translocate CRT on its own (17, 18). Oxaliplatin was also shown to translocate CRT, albeit only when administered at a much higher concentration than in the case of compound **1** and auranofin. Last, the untreated cells showed a small amount of translocation. To quantify the amount of CRT translocation, the experiment was repeated and analyzed by flow cytometry. Dead cells were gated out using SYTOX Blue (*SI Appendix,* Fig. S2). As shown in Fig. 2*D*, flow cytometry analysis confirms that Compound **1** induces more CRT translocation at 10 μM compared to both oxaliplatin at 150 μM and auranofin 10 μM.

Extracellular release of ATP in iKAP cells was assessed in the presence of 5 μM or 10 μM of compound **1**, 150 μM of oxaliplatin, or untreated (Fig. 2*E*). The amount of released ATP in culture supernatants 4 h posttreatment was measured using a luciferin-based assay (Invitrogen A22066). Compound **1** induced higher levels of ATP secretion at 5 μM and 10 μM compared to oxaliplatin at 150 μM and the untreated cells.

HMGB1 secretion into the supernatant was assessed by ELISA using a commercial HMGB1 detection kit (Chondrex, 6010). IKAP cells were treated with either compound **1** at 5 μM or 10 μM or oxaliplatin at 150 μM and incubated for 4 h. After incubation, aliquots of the supernatant were taken and centrifuged to remove dead cells before analysis. As shown in Fig. 2*F*, compound **1** generated a similar amount of HMGB1 at 5 μM as did oxaliplatin at 150 μM. Both compound **1** and oxaliplatin were able to generate higher levels of HGMB1 compared to the untreated cells. Altogether, these results provide support for the notion that compound **1** is a potent inducer of the three ICD biomarkers: CRT translocation, ATP release and HMGB1 secretion.

In Vivo Results with Pretreated Cells. Compound **1** was tested for its ability to promote a long-lived immune response in the iKAP syngeneic immunocompetent mouse model. Oxaliplatin was used as a potential positive control as it had been shown

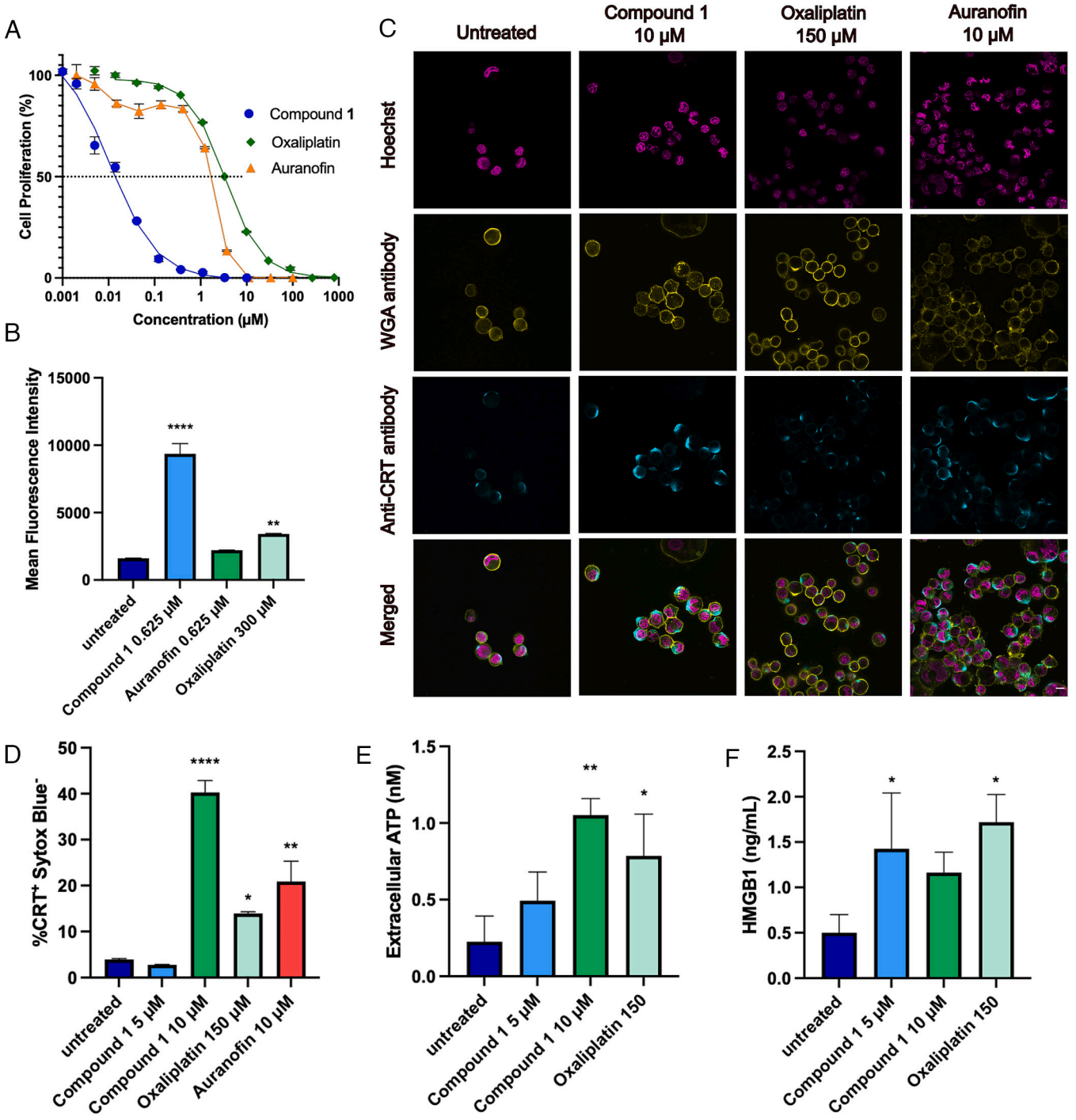

Fig. 2. (*A*) 72-h MTT assay IC_{50} data for compound **1**, oxaliplatin, and auranofin in iKAP cells. (*B*) Flow cytometry studies showing generation of reactive oxygen species in iKAP cells 24 h post treatment vs. untreated cells. (*C*) Confocal microscopy images showing translocation of ER chaperone protein calreticulin (CRT) to the cell surface in the absence of treatment (untreated), as well as after incubation with compounds: **1** at 10 μM, oxaliplatin 150 μM, and auranofin 10 μM. The cells were stained with anti-CRT polyclonal antibodies labeled with Alexa Fluor 594 (colored blue), cell membrane staining WGA antibody (yellow) and nuclear staining Hoechst (purple). (Scale bar is 10 μm.) (Colors of staining were edited in Fiji to help better view the extent of colocalization. (*D*) Results of flow cytometry showing CRT release in iKAP cells 24 h post treatment with **1** vs. untreated, auranofin 10 μM and 150 μM oxaliplatin treated cells. (*E*) ATP release in iKAP cells 4 h post-treatment with **1**, and oxaliplatin vs. untreated. (*F*) Release of extracellular HMGB1 in iKAP cells 4 h post-treatment with **1** or oxaliplatin vs. untreated (one-way ANOVA with Tukey's multiple comparison). Data are mean ± SD and a *P* value < 0.05 is considered statistically significant. **P* < 0.05, ***P* < 0.01, ****P* < 0.001, *****P* < 0.0001.

to induce ICD in a CT26 tumor model at 150 μM. In our study, the iKAP mice (n = 5 to 6 per group) were injected subcutaneously on the right flank with iKAP cells (3×10^6) that were treated with compound **1** at 10 μM or oxaliplatin at 150 μM for 4 h. A concentration of 10 μM was chosen for compound **1** based on the in vitro biomarker results (Fig. 2 *D*–*F*). As a control, untreated iKAP cells were subjected to three freeze–thaw cycles to induce necrosis (expected to be a nonimmunogenic form of cell death). One week later, the mice were challenged subcutaneously in the left flank with naïve, live iKAP cells (5×10^5), and tumor growth was monitored over time. This experimental scheme is illustrated in Fig. 3*A*.

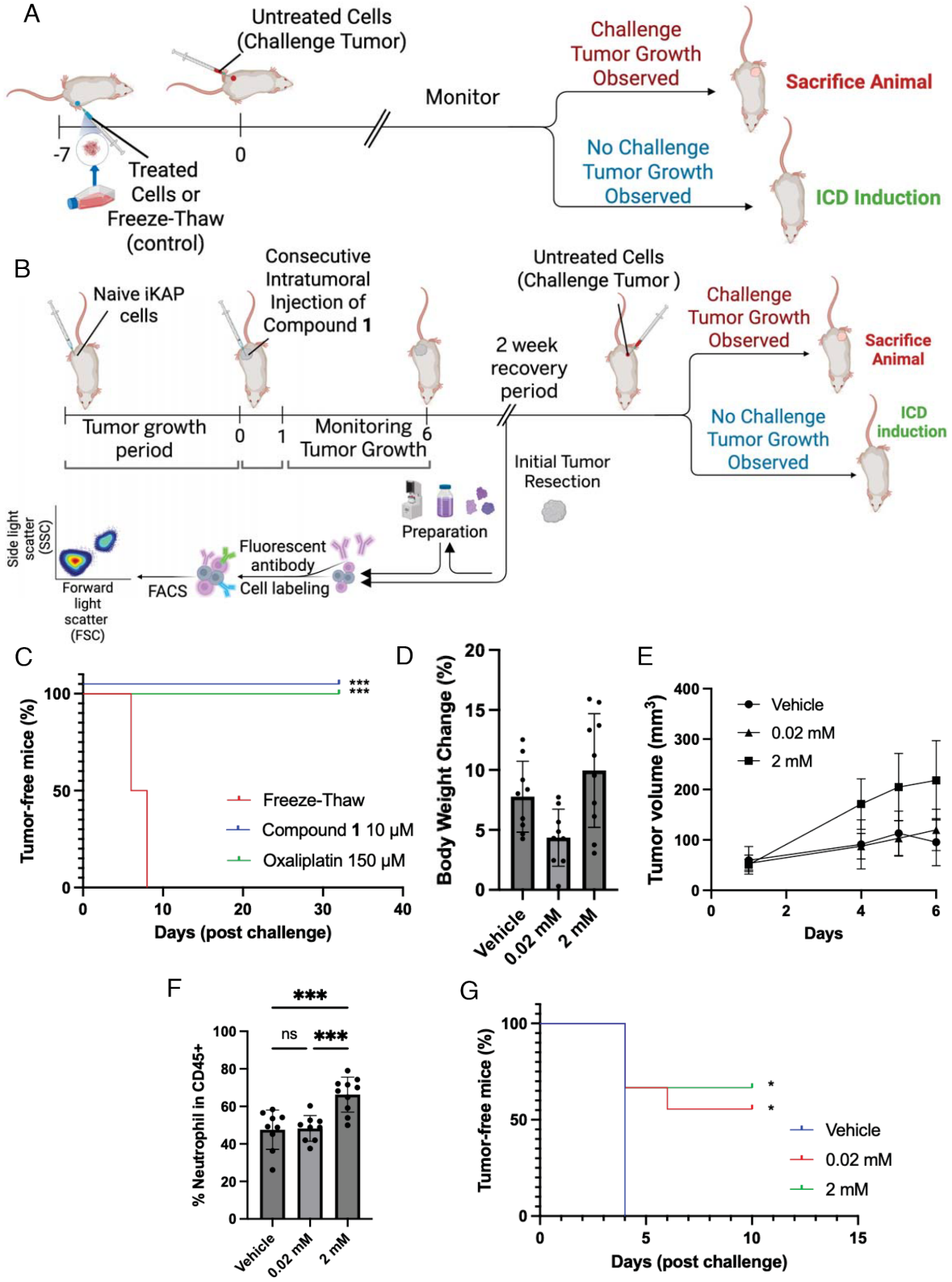

Fig. 3. (*A*) Schematic illustration of in vivo studies of ICD involving pretreated iKAP cells. (*B*) Schematic summary of the Intratumoral ICD experiment, as well as processing and subsequent FACS analysis of the established tumor after treatment. (*C*) Percent tumor-free mice (n = 5 to 6/group) (i.e., left flank tumor) injected with pretreated iKAP cells with either 10 μM of compound **1** (n = 6), 150 μM oxaliplatin (n = 5), or freeze-thaw cells (n = 6) in the right flank and then inoculated (i.e., challenged) with iKAP cells in the left flank. Data points for compound **1** are nudged up by 5 units to avoid overlap with oxaliplatin. Mantel–Cox log-rank test, ***$P < 0.0001$ (Bonferroni-corrected) indicates a statistically significant difference from freeze–thaw. (*D*) Percent body weight change of mice during Intratumoral study. (*E*) Volume of initial tumor after injection of compound **1** or vehicle alone. (*F*) Percent of neutrophil infiltration into established tumor after injection of compound **1** or vehicle out of the total $CD45^+$ population. (one-way ANOVA with Tukey's multiple comparison). Data are mean ± SD and a P value < 0.05 is considered statistically significant. *$P < 0.05$, **$P < 0.01$, ***$P < 0.001$, ****$P < 0.0001$. (*G*) Percent tumor-free mice (i.e., left flank tumor) after Intratumoral injection of compound **1** at 0.02 mM (n = 9) and 2 mM (n = 9), as well as vehicle (n = 6). Mice were challenged 2 wk after surgical removal of the initial tumor to allow for full recovery. Mantel–Cox log-rank test, $P < 0.05$ (Bonferroni-corrected) was considered significant, * indicates a statistically significant difference from freeze–thaw.

As seen in Fig. 3*C*, all mice injected with iKAP cells treated with either compound **1** at 10 μM or oxaliplatin at 150 μM prior to live tumor challenge survived and did not develop challenge tumors while those injected with iKAP cells subjected to freeze-thaw prior to tumor challenge developed challenge tumors by day 8 and succumbed.

In Vivo Results Using Intratumoral Injection. In an effort to model a more clinically relevant protocol, the tumor challenge was repeated in a new cohort of mice in which established iKAP tumors were injected intratumorally with either compound **1** or vehicle (a mixture of ethanol, PEG 400, Tween 80, and 20% saline). This experiment is illustrated in Fig. 3*B*. Briefly, mice were injected with live iKAP cells in the right flank and tumors were allowed to develop to 50 mm^3. Once at that size, 0.02 mM or 2 mM of compound **1** or vehicle were injected intratumorally on two consecutive days. Tumor volume and mice body weight were monitored daily. Six days post Intratumoral injection, the tumor was surgically removed, stained, and subsequently analyzed by flow cytometry (*SI Appendix,* Fig. S3). All mice maintained a healthy body weight throughout the experiment (Fig. 3*D*). The tumor volume of the 2 mM cohort increased more than the vehicle and the 0.02 mM groups (Fig. 3*E*). This does not appear to represent increased tumor growth at this higher concentration; rather, it is more consistent with an inflammatory response, supported by increased neutrophil infiltration in the absence of systemic toxicity (Fig. 3*F*).

After the treated tumor was surgically removed, all mice were allowed to recover for 2 wk. Once recovered, each mouse was challenged with live iKAP cells and challenge tumor development was monitored. As seen in Fig. 3*G*, mice in the vehicle group all developed challenge tumors by day 4. In contrast, 5 out of 9 mice that were treated with compound **1** at 0.02 mM and 6 out of 9 mice treated with compound **1** at 2 mM did not develop tumors. These results confirm the ability of compound **1** to generate a tumor specific immune response following Intratumoral injection at both 0.02 mM and 2 mM concentrations.

RNA Profiling. RNA profiling was carried out in iKAP cells treated with compound **1**, auranofin, and oxaliplatin. Briefly, iKAP cells were treated with each compound for 24 h. RNA was isolated using standard literature procedures followed by Illumina sequencing (19). The Gene Set Enrichment Analysis (GSEA) normalized enrichment scores (NES) database for the top 20 pathways affected by compound **1** using the Hallmark database is shown in Fig. 4*A*. Similar analyses for oxaliplatin and auranofin can be found in the supporting information (*SI Appendix,* Figs. S4 and S5). Pathways with nominal *P*-values less than 0.0001 were deemed to be significant. Beyond the expected redox damage response pathways, i.e., the UV response up, unfolded protein response (UPR) (20), p53 and heme metabolism (21), the other highly upregulated pathways induced by compound **1** were associated with immune/inflammation signaling [IL6 JAK STAT3 signaling (22), PI3K AKT mTOR signaling, TGF beta signaling, interferon gamma response, and mTORC1 signaling (23)]. The top downregulated gene sets were associated with the cell cycle, aerobic respiration, and myogenesis similar to what is often seen in virally infected cells (24, 25). Similar changes in the immune/inflammation signaling pathways were seen for oxaliplatin, whereas the NES for auranofin reflected for the most part a response to cellular damage.

The enrichment map for compound **1** was generated from the C2 reactome database (*SI Appendix,* Fig. S6). Two biological themes stood out. The first cluster, Fig. 4*B*, is organized around glutathione conjugation, cellular metabolism, and oxidative stress management, the classical response to ROS stress (26). The second cluster is organized around interferon response, viral infection, and inflammatory pathways (Fig. 5*A*). The gene sets within this cluster include "Blanco Melo covid19 sars cov2 infection calu3 cells up" (a gene set associated with cellular response to covid19 infection) (27), "Zhang interferon response" (a gene set associated with hepatitis D infection) (28) and "Bowie response to tamoxifen" [a gene set associated with damage by human papillomavirus (HPV)] (29).

A volcano plot of all the genes in the interferon gamma response pathway, for compound **1**, was generated (Fig. 5*B*). Several transcripts associated with viral infections had significant differentially expressed genes: i) Viral recognition gene Ifih1, which encodes for the viral recognition protein MDA5, a protein that functions as an intracellular sensor for viral dsRNA, ii) Several IFN stimulated genes (ISGs), such as Rsad2, which potently inhibits the replication of different viruses (30), Isg20 involved in negative regulation of viral genome replication (31), Irf7, a gene downstream of Ifih1 that encodes a key molecule in type I IFN signaling (32), and Isg15, which causes ISGylation of Ifih1/MDA5 (33), and iii) Chemokines Cxcl10, Ccl5, Ccl7, and Cxcl11 that are associated with recruitment of immune cells and production of an inflammatory response (34–36). Additionally, there are several genes that have increased expression that function as regulators of the immune system. These include IL6, a cytokine that contributes to host defense and tissue injury during viral infection, Socs1 and Socs3, genes that act as negative regulators of cytokine signaling (37), IL10, a cytokine that regulates immune responses by suppressing inflammation (38), and Nfkbia that acts as a regulator for Nuclear factor-kappa-B (NF-κB) (39). Also increased was Ptgs2, a gene that produces prostaglandins, which has been linked to other compounds that promote an anti-tumor immune response (40). Consistent with the RNA profiling results, western blot analyses confirmed increased MDA5 protein expression after treatment with compound **1** (*SI Appendix,* Fig. S7). Only the soluble version or cleaved version of MDA5 was detected by western blot (41).

GSEA was performed on Gene Ontology (GO) Biological Process terms (Fig. 5*C*). The top enriched pathways from this analysis were antigen presentation through MHC class 1, endogenous peptide antigen, MHC class 1b, and transporter associated with antigen presentation (TAP)-independent (42). An upregulation in pathways related to exosomal secretion was also seen, as was an increase in the positive regulation of protein polyubiquitination, an activity directly related to proteasome processing for MHC-I peptides. Natural killer cell differentiation was also increased (43). Collectively, these data provide support for the notion that compound **1** induces strong type I interferon induced MHC-I antigen presentation through oxidative stress.

A z-score based heatmap was made using genes associated with the overall activation of the immune system, including UPR, ER stress, and viral recognition (Fig. 5*D*). The genes associated with the UPR through the protein kinase R-like endoplasmic reticulum kinase (PERK) pathway (Ddit3, Atf4, Atf3, Chac1) and the ATF6 pathway (Atf6, Xbp1) were all upregulated in a statistically significant manner, as was ER stress (Hspa1a, Hspa5, Hsp90ab1) (20). Genes directly associated with viral recognition, namely Ifih1 and Isg20, were likewise increased significantly. An increase in the expression of the ISG Irf7 was seen along with a number of chemokines including Cxcl10 and Ccl5. Additionally, Stat1 was found to be downregulated while Stat2 was upregulated. This is indicative of increased sensitivity to chemotherapy and antiviral immunity (44, 45). Finally, an increase in the regulatory genes, Nfkbia, IL10, Socs1, and Socs3 was seen. Taken together, these

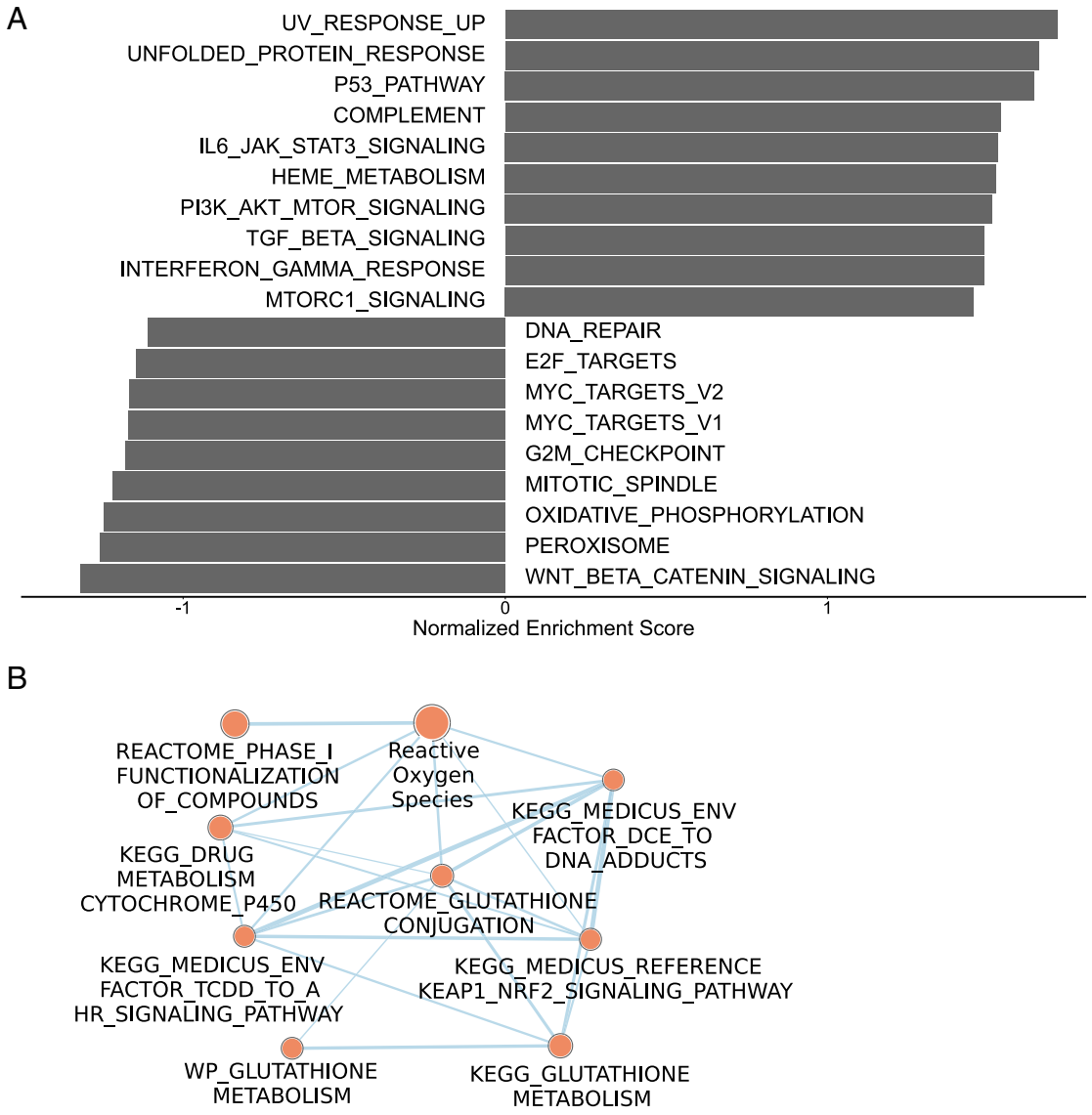

Fig. 4. (*A*) Normalized enrichment scores (NES) from GSEA pathway analysis revealed pathways most affected when iKAP cells are treated with compound **1** vs. untreated cells. Nominal *P*-values less than 0.0001 were deemed to be significant. (*B*) Enrichment map highlighting ROS associated pathways. Shown is a selected portion of the enrichment map generated in Cytoscape from GSEA results using the C2 Reactome database. The network visualization depicts the connectivity between the ROS pathway and glutathione conjugation/metabolism, illustrating their functional overlap and shared gene signatures in the dataset.

findings provide evidence for UPR coupled to ER stress that triggers a response that mimics a well-balanced antiviral state. Our working model based on all of this information is summarized in Fig. 5*E*.

Discussion

The antiviral hallmarks elicited by compound **1** provide a rationale for why this cytotoxic agent gives rise to a strong *anti-tumor immune response* in vivo in both of the challenge study formats investigated (Fig. 3 *C* and *G*). When mice were injected with iKAP cells pretreated with compound **1** 6/6 mice rejected the challenge tumor. Control mice injected with freeze/thaw cells all developed challenge tumors by day 8. These results lead us to conclude that injecting mice with dying iKAP cells pretreated with compound **1** engenders a strong tumor-specific immune response. Moreover, when compound **1** was administered intratumorally at 0.02 mM and 2 mM concentrations in preestablished tumors, 5 out of 9 mice and 6 out of 9 mice did not develop challenge tumors respectively. All control mice injected intratumorally with only vehicle developed challenge tumors by day four. Therefore, even existing tumors injected with compound **1** were able to elicit a protective immune response in the majority of mice tested.

During the Intratumoral study all mice maintained a healthy body weight (i.e., within 15% of their original weight). However, mice whose tumors were injected with the 2 mM concentration of compound **1** exhibited larger tumor volumes compared to the 0.02 mM and vehicle control groups. This increase in tumor volume coincided with increased neutrophil infiltration, leading us to suggest that the increase in tumor volume was not due to actual tumor growth but rather inflammation caused by an increase in neutrophils.

The ROS assay verified that compound **1** generates ROS effectively (Fig. 2*B*), presumably through the simultaneous redox cycling of the naphthoquinone moiety and inhibition of TrxR2 with Au(I). It proved more cytotoxic than auranofin, which only inhibits TrxR2 (Fig. 2*A*). We thus suggest that the ROS generated by the naphthoquinone moiety present in **1** (but not auranofin)

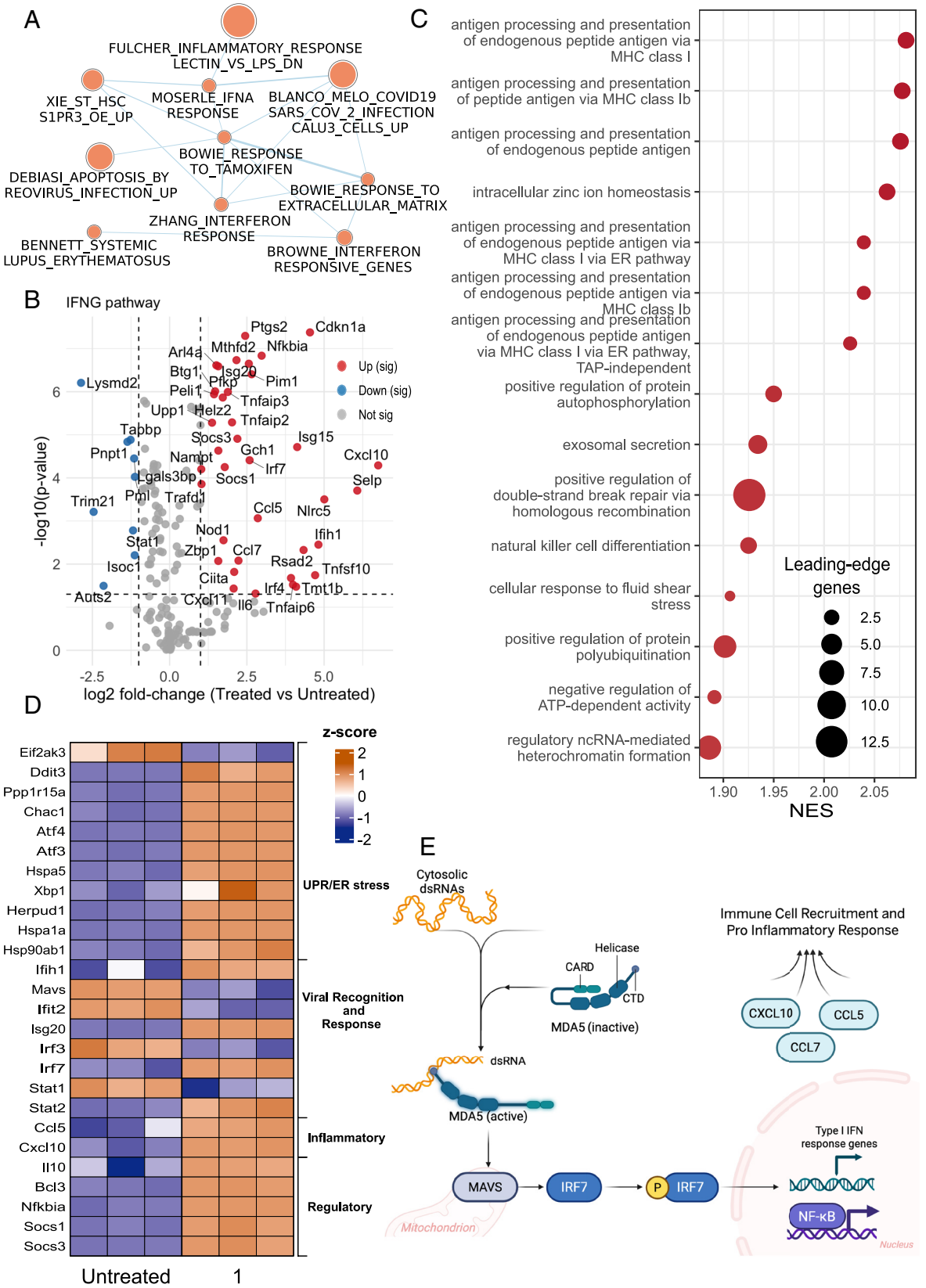

Fig. 5. (*A*) Enrichment map highlighting interferon response–associated pathways. What is shown is a selected portion of the enrichment map generated in Cytoscape from the GSEA results using the C2 Reactome database. The network visualization depicts the connectivity of the interferon response gene sets and highlights their shared enrichment in pathways linked to inflammatory response resulting from viral infection. (*B*) Volcano plot of log2FC vs. -$\log_{10}$(*P*-value) for genes in the interferon gamma response pathway. log2FC calculated with pseudocount to handle zero counts. Genes that are upregulated are shown in red and genes that are down regulated are shown in blue. Genes that were not statistically significant are shown in gray. The dashed line represents the cut off for statistical significance ($P < 0.05$). (*C*) GO Biological Processing Terms from GSEA using *clusterProfiler/fgsea* with [rank metric], minSize = 10 (or 15), maxSize = 500. (*D*) Heatmap showing the distribution of log2 normalized expression of iKAP cells untreated vs. compound **1** by Z-score. (*E*) Working model for how compound **1** overcomes "self-tolerance" of the immune system and causes the generation of a controlled viral mimicry effect. Created in BioRender. Levine (5) (https://BioRender.com/6meiwep).

is largely responsible for the observed increase in cytotoxicity. Consistent with this interpretation, the RNA profiling enrichment map revealed ROS associated pathways in the case of compound **1** (Fig. 4*B*). For example, compound **1** activates the NRF2 signaling pathway, presumably because it inhibits TrxR2. This, in turn, leads to an increase in the expression of glutathione (GSH), which can act as a "redox buffer" helping to mitigate ROS damage (26). On the other hand, compound **1** is cytotoxic. Thus, we suggest that the increased GSH levels are not able to keep up with ROS-induced stress, which leads eventually to cell death.

As shown in Fig. 5*B*, compound **1** caused an approximately 50-fold increase in the expression of Ifih1. This is among the most upregulated genes. Ifih1 encodes for the protein MDA5, a cytosolic RNA sensor that specifically recognizes dsRNA. The upregulation of Ifih1 therefore provides indirect evidence that dsRNA is being formed and released into the cytosol of the cell in the presence of compound **1**. ROS damage within the mitochondria, where compound **1** localizes, can result in the formation of dsRNA. While dsRNA species were not directly visualized in this study, prior work has shown that mitochondrial oxidative stress is sufficient to generate immunogenic dsRNA capable of engaging MDA5-dependent antiviral pathways (46).

In addition, the NES for iKAP cells treated with compound **1** showed the UPR pathway gene set was the 2nd most upregulated (Fig. 4*A*). This is reinforced by the heatmap shown in Fig. 5*D* where the genes associated with subsets of the UPR pathway; the PERK pathway, and the ATF6 pathway, have z-scores that are the most increased in the presence of compound **1** relative to untreated iKAP cells. In chemotherapy-induced ICD (e.g., anthracyclines, oxaliplatin), ER stress typically leads to PERK-dependent phosphorylation of eIF2α without activation of ATF4 or the IRE1/XBP1 axis, resulting in only partial CRT exposure. Moreover, activation of the IRE1/XBP1 pathway has been shown to inhibit CRT exposure and abolish ICD (47). Compound **1** differs in that all three pathways of the UPR are at least partially activated and compound **1** is still able to induce ICD. Upregulation of this pathway is known to occur in response to an accumulation of misfolded proteins, which triggers ER stress (48). It has been shown that ROS damage can cause protein misfolding by direct oxidation of amino acid residues (48). Therefore, as it pertains to compound **1**, it is reasonable to conclude that the ROS generated causes the misfolding of proteins resulting in ER stress and upregulation of the UPR pathway.

Rosenburg et al have discussed how doxorubicin as well as DMT1 inhibitors decitabine and 5-aza; HMT inhibitors GSK126, GSK343, and UNC1999; MDM2 inhibitor Nutlin 7041 have also been shown to activate the UPR pathway in cancer cells (49). In the case of these other agents, it has been widely reported that there is also upregulation of viral recognition sensors, such as TLR3, RIG-I, ZBP1, LGP2, PKR, and MDA5 (49). Recall that the gene that encodes MDA5 was also strongly upregulated upon treatment with compound **1**. These viral recognition sensors lead to downstream ISG production and transcription of type I IFNs, along with upregulation of chemokines including Ccl5 and Cxcl10. These same signaling events occur upon viral infection of cells. That is why the downstream immune response to compounds, such as doxorubicin, as well as the response generated by DMT1, HMT, and MDM2 inhibitors, has often been compared to that seen in cells that are virally infected, a phenomenon referred to as "viral mimicry" (15).

Compound **1** triggers increased expression of MDA5. It also upregulates the UPR pathway. We thus suggest that compound **1** elicits a transcriptional and innate immune response consistent with viral mimicry. Evidence in support of this proposition is inferred from coordinated activation of MDA5 and the observed increase in its downstream ISG Irf7. Additionally, the activation of antigen presentation and upregulation of chemokines that have a direct role in the adaptive immune response, such as Cxl10, further supports this hypothesis (50). Also noteworthy is the fact that the cellular response induced by compound **1** in iKAP cells (as reflected in the enrichment map) overlaps with the cellular responses to cells infected with viruses, such as COVID-19 and HPV (Fig. 5*A*). The net result is activation of the innate immune response, which occurs in concert with recruiting immune cells that lead to an adaptive immune response.

In the iKAP cells, compound **1** was able to generate all three biomarkers (CRT, ATP, and HMGB1) traditionally associated with ICD. While auranofin also caused a small increase in CRT translocation, it failed to induce the antiviral transcriptional program observed with compound **1**. It is important to note that the measured concentrations of ATP and HGMB1 in the iKAP cell line after compound **1** treatment were much lower than what we previously reported for the same compound in a CT26 CRC cell line. Nevertheless, compound **1** elicited a strong tumor specific immune response in this iKAP model. Taken together, our findings lead us to suggest that activation of antiviral signaling pathways may complement or, in some contexts substitute for, canonical ICD markers such as ATP and HMGB1 in driving effective antitumor immunity.

Conclusion

Viral mimicry may be playing a larger role in regulating the treatment efficacy of cytotoxic agents than is currently appreciated. While most compounds previously reported to induce viral mimicry did so through direct inhibition or activation of DNA editing machinery, compound **1** causes this to occur indirectly through ROS generation. Production of ROS by compound **1** leads to the accumulation of misfolded proteins and the generation of dsRNA as described above. The common feature is that both of these mechanisms activate viral infection recognition sensors, such as MDA5. They also cause an increase in the UPR pathway resulting in ER stress. We suggest that many other cytotoxic agents in addition to compound **1** will induce similar effects. In particular, it may turn out that other types of damage beyond ROS culminate in activation of an innate and adaptive immune response initiated through different viral recognition sensors.

It has long been seen that different patients treated with the same chemotherapeutic experience different outcomes. We speculate that in certain cases the cytotoxicity of the chemotherapeutic does not suffice to kill all the cancer cells, yet a favorable response is still seen. While demonstrated here using a redox-active Au(I) complex, these findings support a broader framework in which mitochondrial oxidative stress can couple cytotoxic injury to antiviral innate immune signaling. Extrapolating from our findings, we propose that individual-by-individual engagement of an adaptive immune response involving viral mimicry plays a key role in mediating the most positive outcomes. To the extent this proposition proves true, the key could be to find new ways to trigger viral mimicry in the case of established anticancer agents. One way this could potentially be done would be to administer the agents at relatively low levels so as to drive a tumor specific immune response before cytotoxicity effects lead to cell death. It will likely also be important to minimize damage to patients' immune systems during treatment. Clinical tests of this hypothesis, if supportive of our suggestion, are expected to translate into new protocols that could improve patient outcomes.

Materials and Methods

Compound **1** was synthesized and characterized as previously described (5). Oxaliplatin (FD26607) was purchased from Biosynth and Auranofin (A6733) was purchased from Sigma Aldrich. Antibodies were either purchased from Biolegend, ThermoFisher, or Invitrogen as described in *SI Appendix*. IKAP cells were provided by coauthor Ronald DePinho's laboratory at the MD Anderson Cancer Center. The cultured iKAP cell lines were generated as previously described (12). GSEA was performed using GSEA_4.4.0 and C2 reactome enrichment map was generated in Cytoscape v3.10.3. In vitro and in vivo experimental details are provided in *SI Appendix*.

Data, Materials, and Software Availability. RNA profiling data have been deposited in NCBI's Gene Expression Omnibus (GEO) and are accessible through GEO Series accession number GSE319636 (https://www.ncbi.nlm.nih.gov/geo/query/acc.cgi?acc=GSE319636) (51).

ACKNOWLEDGMENTS. This work was supported by the US NIH (CA068682 to J.L.S.), the Robert A. Welch Foundation (F-0018 to J.L.S.) Additional support was provided by the UT Austin/MD Anderson Cancer Center Collaborative Pilot Project Grant. Figures were partially created with Biorender.com. J.L. was supported by the Odyssey Fellowship Program of the University of Texas MD Anderson Cancer Center and CFP foundation. The MDACC Advanced Microscopy Core is supported by NIH S10 RR029552. The MDACC Advanced Cytometry & Sorting Core Facility is supported by NCI P30CA016672. R.A.D. is supported by MD Anderson Start Up funds and the Harry Graves Burkhart III Distinguished University Chair in Cancer Research. Data were generated in part through the use of the Advanced Technology Genomics Core (ATGC), which receives partial support from the National Cancer Institute under grant P30CA016672 to MD Anderson Cancer Center. The research reported in this publication was not directly funded through the P30CA016672 grant to MD Anderson Cancer Center and is not within the scope of such grant.

1. L. Galluzzi *et al.*, Consensus guidelines for the definition, detection and interpretation of immunogenic cell death. *J. Immunother. Cancer* **8**, e000337 (2020).
2. N. Casares *et al.*, Caspase-dependent immunogenicity of doxorubicin–induced tumor cell death. *J. Exp. Med.* **202**, 1691 (2005).
3. C. Li *et al.*, Mitoxantrone triggers immunogenic prostate cancer cell death via p53-dependent PERK expression. *Cell. Oncol.* **43**, 1099–1116 (2020).
4. K.-B. Huang *et al.*, Cu(II) complex that synergistically potentiates cytotoxicity and an antitumor immune response by targeting cellular redox homeostasis. *Proc. Natl. Acad. Sci. U.S.A.* **121**, e2404668121 (2024).
5. M. S. Levine *et al.*, Long-lived immunogenic cell death induced by a water-soluble redox active Au(I) bis-N-heterocyclic carbene. *J. Am. Chem. Soc.* **147**, 23574–23582 (2025).
6. S. Sen *et al.*, Metal-based anticancer agents as immunogenic cell death inducers: The past, present, and future. *Chem. Soc. Rev.* **51**, 1212–1233 (2022).
7. Y. Lu *et al.*, Oxoisoaporphine alkaloid iridium(III) derivative: An immunogenic cell death inducer that engages the autophagy-dependent regulator cathepsin D. *J. Am. Chem. Soc.* **147**, 15216–15228 (2025).
8. C. Ma *et al.*, Nanomaterials: Leading immunogenic cell death-based cancer therapies. *Front. Immunol.* **15**, 1447817 (2024).
9. Y.-Y. Wu, T.-K. Sun, M.-S. Chen, M. Munir, H.-J. Liu, Oncolytic viruses-modulated immunogenic cell death, apoptosis and autophagy linking to virotherapy and cancer immune response. *Front. Cell. Infect. Microbiol.* **13**, 1142172 (2023).
10. D. V. Krysko *et al.*, Immunogenic cell death and DAMPs in cancer therapy. *Nat. Rev. Cancer* **12**, 860–875 (2012).
11. P. J. Barnard, S. J. Berners-Price, Targeting the mitochondrial cell death pathway with gold compounds. *Coord. Chem. Rev.* **251**, 1889–1902 (2007).
12. A. T. Boutin *et al.*, Oncogenic Kras drives invasion and maintains metastases in colorectal cancer. *Genes Dev.* **31**, 370–382 (2017).
13. J. Li, X. Ma, D. Chakravarti, S. Shalapour, R. A. DePinho, Genetic and biological hallmarks of colorectal cancer. *Genes Dev.* **35**, 787–820 (2021).
14. W. Liao *et al.*, KRAS-IRF2 axis drives immune suppression and immune therapy resistance in colorectal cancer. *Cancer Cell* **35**, 559–572.e7 (2019).
15. D. Roulois *et al.*, DNA-demethylating agents target colorectal cancer cells by inducing viral mimicry by endogenous transcripts. *Cell* **162**, 961–973 (2015).
16. Y. Zhang *et al.*, Zebularine potentiates anti-tumor immunity by inducing tumor immunogenicity and improving antigen processing through cGAS-STING pathway. *Commun. Biol.* **7**, 587 (2024).
17. L. Freire Boullosa *et al.*, Auranofin reveals therapeutic anticancer potential by triggering distinct molecular cell death mechanisms and innate immunity in mutant p53 non-small cell lung cancer. *Redox Biol.* **42**, 101949 (2021).
18. J. V. Loenhout *et al.*, Auranofin and Cold Atmospheric Plasma synergize to trigger distinct cell death mechanisms and immunogenic responses in glioblastoma. *Cells* **10**, 2936 (2021).
19. J. F. Arambula *et al.*, Targeting antioxidant pathways with ferrocenylated N-heterocyclic carbene supported gold(I) complexes in A549 lung cancer cells. *Chem. Sci.* **7**, 1245–1256 (2016).
20. M. I. Mohd Ropidi, A. S. Khazali, N. Nor Rashid, R. Yusof, Endoplasmic reticulum: A focal point of Zika virus infection. *J. Biomed. Sci.* **27**, 27 (2020).
21. W. Xia, P. Jiang, P53 promotes antiviral innate immunity by driving hexosamine metabolism. *Cell Rep.* **43**, 113724 (2024).
22. S. Liu *et al.*, STAT3 regulates antiviral immunity by suppressing excessive interferon signaling. *Cell Rep.* **42**, 112806 (2023).
23. P. J. Mullen *et al.*, SARS-CoV-2 infection rewires host cell metabolism and is potentially susceptible to mTORC1 inhibition. *Nat. Commun.* **12**, 1876 (2021).
24. X. Liu, L. Lou, L. Zhou, Molecular mechanisms of cardiac injury associated with myocardial SARS-CoV-2 infection. *Front. Cardiovasc. Med.* **8**, 643958 (2022).
25. A. Lopez *et al.*, Viral modulation of the DNA damage response and innate immunity: Two sides of the same coin. *J. Mol. Biol.* **434**, 167327 (2022).
26. M. Jaganjac, L. Milkovic, S. B. Sunjic, N. Zarkovic, The NRF2, thioredoxin, and glutathione system in tumorigenesis and anticancer therapies. *Antioxidants* **9**, 1151 (2020).
27. D. Blanco-Melo *et al.*, Imbalanced host response to SARS-CoV-2 drives development of COVID-19. *Cell* **181**, 1036–1045.e9 (2020).
28. Z. Zhang *et al.*, Hepatitis D virus–induced interferon response and administered interferons control cell division–mediated virus spread. *J. Hepatol.* **77**, 957–966 (2022).
29. M. L. Bowie *et al.*, Interferon regulatory factor-1 regulates reconstituted extracellular matrix (rECM)-mediated apoptosis in human mammary epithelial cells. *Oncogene* **26**, 2017–2026 (2007).
30. E. S. Lim, L. I. Wu, H. S. Malik, M. Emerman, The function and evolution of the restriction factor viperin in primates was not driven by lentiviruses. *Retrovirology* **9**, 55 (2012).
31. Z. Chen, M. Yin, H. Jia, Q. Chen, H. Zhang, ISG20 stimulates anti-tumor immunity via a double-stranded RNA-induced interferon response in ovarian cancer. *Front. Immunol.* **14**, 1176103 (2023).
32. W. Ma, G. Huang, Z. Wang, L. Wang, Q. Gao, IRF7: Role and regulation in immunity and autoimmunity. *Front. Immunol.* **14**, 1236923 (2023).
33. Y.-C. Perng, D. J. Lenschow, ISG15 in antiviral immunity and beyond. *Nat. Rev. Microbiol.* **16**, 423–439 (2018).
34. R. E. Marques, R. Guabiraba, R. C. Russo, M. M. Teixeira, Targeting CCL5 in inflammation. *Expert Opin. Ther. Targets* **17**, 1439–1460 (2013).
35. J. R. Groom, A. D. Luster, CXCR3 in T cell function. *Exp. Cell Res.* **317**, 620–631 (2011).
36. M. Zhang *et al.*, CCL7 recruits cDC1 to promote antitumor immunity and facilitate checkpoint immunotherapy to non-small cell lung cancer. *Nat. Commun.* **11**, 6119 (2020).
37. N. P. D. Liau *et al.*, The molecular basis of JAK/STAT inhibition by SOCS1. *Nat. Commun.* **9**, 1558 (2018).
38. V. Carlini *et al.*, The multifaceted nature of IL-10: Regulation, role in immunological homeostasis and its relevance to cancer, COVID-19 and post-COVID conditions. *Front. Immunol.* **14**, 1161067 (2023).
39. D. C. Scherer, J. A. Brockman, Z. Chen, T. Maniatis, D. W. Ballard, Signal-induced degradation of I kappa B alpha requires site-specific ubiquitination. *Proc. Natl. Acad. Sci. U.S.A.* **92**, 11259–11263 (1995).
40. C. R. Bell *et al.*, Chemotherapy-induced COX-2 upregulation by cancer cells defines their inflammatory properties and limits the efficacy of chemoimmunotherapy combinations. *Nat. Commun.* **13**, 2063 (2022).
41. M. Okamoto *et al.*, Soluble form of the MDA5 protein in human sera. *Heliyon* **10**, e31727 (2024).
42. N. Pishesha, T. J. Harmand, H. L. Ploegh, A guide to antigen processing and presentation. *Nat. Rev. Immunol.* **22**, 751–764 (2022).
43. N. K. Björkström, B. Strunz, H.-G. Ljunggren, Natural killer cells in antiviral immunity. *Nat. Rev. Immunol.* **22**, 112–123 (2022).
44. S. Wang *et al.*, A feedforward loop between STAT1 and YAP1 stimulates lipid biosynthesis, accelerates tumor growth, and promotes chemotherapy resistance in mutant KRAS colorectal cancer. *Commun. Biol.* **8**, 1278 (2025).
45. X. Li *et al.*, Initial activation of STAT2 induced by IAV infection is critical for innate antiviral immunity. *Front. Immunol.* **13**, 960544 (2022).
46. A. Dhir *et al.*, Mitochondrial double-stranded RNA triggers antiviral signalling in humans. *Nature* **560**, 238–242 (2018).
47. O. Kepp, L. Bezu, G. Kroemer, The endoplasmic reticulum chaperone BiP: A target for immunogenic cell death inducers? *Oncoimmunology* **11**, 2092328 (2022).
48. D. Ron, P. Walter, Signal integration in the endoplasmic reticulum unfolded protein response. *Nat. Rev. Mol. Cell Biol.* **8**, 519–529 (2007).
49. L. Rosenberg, N. Vabret, Viral mimicry in cancer therapy. *Trends Cancer* **11**, 1185–1202 (2025), 10.1016/j.trecan.2025.08.010.
50. A. Sistigu *et al.*, Cancer cell–autonomous contribution of type I interferon signaling to the efficacy of chemotherapy. *Nat. Med.* **20**, 1301–1309 (2014).
51. M. S. Levine *et al.*, Viral mimicry may help explain immunogenic cell death. National Center for Biotechnology Information Gene Expression Omnibus. https://www.ncbi.nlm.nih.gov/geo/query/acc.cgi?acc=GSE319636. Deposited 17 February 2026.